Biosensors and Bioelectronics 236 (2023) 115437

Contents lists available at ScienceDirect

Biosensors and Bioelectronics

journal homepage: www.elsevier.com/locate/bios

Zirconium dioxide as electrochemiluminescence emitter for D-dimer determination based on dual-quenching sensing strategy

Xue Dong [a], Xiaoyue Zhang [a], Yu Du [a], Jiajun Liu [a], Qingze Zeng [a], Wei Cao [a], Qin Wei [a,b,*], Huangxian Ju [c]

[a] Key Laboratory of Interfacial Reaction & Sensing Analysis in Universities of Shandong, Collaborative Innovation Center for Green Chemical Manufacturing and Accurate Detection, School of Chemistry and Chemical Engineering, University of Jinan, Jinan, 250022, PR China
[b] Department of Chemistry, Sungkyunkwan University, Suwon, 16419, Republic of Korea
[c] State Key Laboratory of Analytical Chemistry for Life Science, School of Chemistry and Chemical Engineering, Nanjing University, Nanjing, 210023, PR China

ARTICLE INFO

Keywords:
Zirconium dioxide
Co-reaction accelerator
Dual-quenching
D-dimer
Peptide ligands

ABSTRACT

The ECL emission of simple and stable zirconium dioxide nanomaterials has always been a blank slate in the ECL sensors field. In this work, zirconium dioxide (ZrO_2)-titanium dioxide (TiO_2)-gold nanoparticle (AuNPs) composite (ZT-Au), a novel self-enhanced ECL emitter, was introduced the system of dual-quenching ECL immunosensor. The anodic luminescence of ZrO_2 in the system of tripropylamine (TPrA) as a co-reagent was first reported and explored. Meanwhile, TiO_2 was designed into the ECL scheme as a co-reaction accelerator to form the ZrO_2/TPrA/TiO_2 ternary system, which can efficiently amplify the ECL signal of the emitter. In addition, cuprous oxide-triaminophenol (Cu_2O-APF) as the quencher was devoted to the dual-quenching sensing strategy. The dual-quenching mechanism that effectively boosted the immunosensor sensitivity was adequately investigated and conjectured in this paper. The sensing model based on the luminophor ZT-Au and the quencher Cu_2O-APF was utilized for the detection of D-dimer, a reliable marker for the diagnosis and evaluation of thrombotic diseases. The short peptide ligands NARKFYKGC (NFC) with efficient biological affinity were used to site-directionally capture antibodies for adequately protecting the activity of antigen binding sites during the construction of the immunosensor. The implemented immunosensor was equipped with a broad linear range of 0.01–500 ng/mL and a low detection limit of 3.6 pg/mL. The original methodology opens up the field of vision for the detection of additional biomarkers.

1. Introduction

Electrochemiluminescence (ECL) is a phenomenon in which the luminophor applied to a certain voltage forms an excited state through a series of reactions to produce ECL emission. In contrast to fluorescence (Li et al., 2021; Liu et al., 2022; Qu et al., 2022), ECL has nearly no background interference due to the absence of an external light source. ECL has better control and regulation of the optical signal of emitter compared with chemiluminescence (Kagalwala et al., 2022; Yu and Zhao, 2021). Therefore, ECL is widely used in numerous fields such as imaging, biological analysis, environmental detection, clinical diagnosis (Ma et al., 2020; Mohan et al., 2022; Sabzehmeidani and Kazemzad, 2022; Sobhanie et al., 2022; Tian et al., 2021; Yuan et al., 2021).

D-dimer has been identified as a reliable marker for the diagnosis and evaluation of thrombosis as the degradation product of cross-linked fibrin. Fibrinolysis in the body is vibrant once the D-dimer level rises, indicating the formation of blood clots such as deep vein thrombosis and pulmonary embolism (Ordieres-Ortega et al., 2020). Furthermore, D-dimer can be used to monitor the disease progression of COVID-19 (Favaloro and Thachil, 2020; Zhao et al., 2021). Studies have shown that severe COVID-19 patients have higher levels of D-dimer than mild patients. The application of the ECL immunosensor to the detection of D-dimer can show favorable sensitivity, specificity and accuracy.

The continued exploitation of luminophor has been a crucial prerequisite for keeping the ECL alive in various fields. Metallic oxide semiconductor materials typically exhibit clumpy structures and stable properties, which make them difficult to use in the ECL field. However, the conversion of semiconductor materials from bulk to nanoscale has

* Corresponding author. Key Laboratory of Interfacial Reaction & Sensing Analysis in Universities of Shandong, Collaborative Innovation Center for Green Chemical Manufacturing and Accurate Detection, School of Chemistry and Chemical Engineering, University of Jinan, Jinan, 250022, PR China.
E-mail address: sdjndxwq@163.com (Q. Wei).

https://doi.org/10.1016/j.bios.2023.115437
Received 17 January 2023; Received in revised form 4 May 2023; Accepted 26 May 2023
Available online 26 May 2023

led to a qualitative change in their optical, physical, electrochemical and other properties, which is commonly referred to as "quantum size effect" (Zhao et al., 2022). This phenomenon makes it possible for metallic oxide semiconductor nanomaterials to possess ECL properties. Zirconium dioxide (ZrO_2) nanomaterials have been reported in energy storage, photocatalysis, adsorption and fluorescence (Adebayo et al., 2022; Huang et al., 2021; Silva et al., 2021; Winczewski et al., 2022; Yang et al., 2022), but seldom reported as ECL emitters. In this work, the anodic luminescence properties of ZrO_2/tripropylamine (TPrA) were researched for the first time. In addition, Titanium dioxide (TiO_2) and gold nanoparticle (AuNPs) were introduced into the luminescence system. TiO_2 was considered as a co-reaction accelerator reacting with TPrA to promote the production of intermediates that boosted the ECL response of ZrO_2 (Hu et al., 2020; Jia et al., 2019). The presence of AuNPs largely enhanced the conductivity and electron transport efficiency of the emitter (Cui et al., 2018). The ternary system ZrO_2/TPrA/TiO_2-AuNPs is known to have high-performance luminescence and stabilized emission. As an ECL emitter, ZrO_2–TiO_2-AuNPs (ZT-Au) provided the eminent sensing platform for immunosensor construction and target detection.

The fabrication of immunosensors relies primarily on the specific identification of antigens and antibodies to complete the quantitative analysis of the target (Li et al. 2020, 2022; Rao et al., 2022). In essence, the efficient identification of biomolecules is the key factor affecting the sensitivity of the sensor. In general, it is difficult to determine the morphology of the antibody on the electrode surface, which may be inverted, horizontal or vertical on the solid surface. However, only antibodies in the vertical state can efficiently recognize the antigen. The strategy of improving antigen recognition by directional coupling of antibodies is crucial in the construction of immunosensors (Ledsgaard et al., 2022; Sueda, 2022; Ye et al., 2021). Polypeptides that can orientally connect to the Fc portion of the antibody are introduced into the immunosensor to maximize the ideal state of the antibody and maintain the activity of the Fab fragment that can trap the antigen. Based on this principle, the short peptide ligand NARKFYKGC (NFC) was introduced to achieve the targeted immobilization of antibodies and improve the recognition and sensitive detection of target molecules (Lupu et al., 2021; Sugita et al., 2013).

Appropriate fabrication strategies such as quenching or enhancement can significantly boost the sensitivity and specificity of the sensor (Chen and Hildebrandt, 2020; Jin et al., 2020; Tian et al., 2023; Wei et al., 2022). Quenchers with superior quenching efficiency have also been extensively developed and studied. In this paper, cuprous oxide-triaminophenol (Cu_2O-APF), a dual-quenching quencher, was designed as a secondary antibody (Ab_2) marker. The matched energy levels of Cu_2O and ZT-Au provided the possibility of electron transfer leading to a quenching of the emitter (Gao et al., 2021). In addition, the benzoquinone on the APF could react with the reduction state of ZrO_2 generated in the luminescence process to secondary quench the ECL signal of the emitter. The dual-quenching strategy could ensure the high-efficiency quenching and considerably improve the sensitivity of the immunosensor.

2. Experimental

2.1. Preparation of ZT-Au

First, SiO_2 microspheres were synthesized as templates by seed growth. 80 mL of ethanol, 4.85 mL of ultrapure water and 3.6 mL of ammonia solution were placed in a 250 mL round-bottom flask in order, then stirred and heated to 55 °C. 3.1 mL of TEOS and 8 ml ethanol was quickly added to the above solution and stirred at 55 °C for 5 h, which was the seed solution. 10 mL of seed solution, 70 mL of ethanol, 13 mL of ultrapure water and 7.5 mL of ammonia solution were mixed and heated to 55 °C. Subsequently, 1 mL of TEOS and 10 mL of ethanol were added and stirred continuously for 5 h. The resulting SiO_2 microspheres were centrifuged and washed with ethanol for several times.

1.2 mL of sodium citrate (48 mg) and 225 μL of $HAuCl_4$ (2%) was added to the SiO_2 solution and stirred for 10 min until dissolved. Then $NaBH_4$ solution was added drop by drop and stirred for 2 h to obtain Au–SiO_2 colloid. The Au–SiO_2 was collected after washing and drying for subsequent use.

0.5 mL of TBOT was dispersed in 20 mL ethanol and sonicated for 20 min, then 286 μL of zirconium n-butoxide was added and sonicated again for 30 min 100 mg of Au–SiO_2 was added into the mixed solution and sonicated for 30 min. The mixture of ultrapure water and ethanol (50 mL/10 mL) was added into the above solution drop by drop under stirring. The mixture was stirred vigorously for 8 h and the obtained product ZrO_2–TiO_2–SiO_2–Au was dried and collected after centrifugation and washing.

100 mg of ZrO_2–TiO_2–SiO_2–Au was dissolved in 20 mL of sodium hydroxide (0.4 g) solution and stirred at 90 °C for 4 h. The product ZT-Au was achieved by washing and drying.

2.2. Preparation of Cu_2O-APF

First, Cu_2O nanospheres were synthesized according to literature and the specific steps are as follows (Luo et al., 2020): 2 mL of sodium hydroxide (80 mg) aqueous solution was added to 25 mL of EG containing 50 mg of copper acetate that has been preheated to 60 °C. 50 mg of D-(+)-glucose powder was added to the solution that was violently stirred to dark blue. The transformation of the mixture from green to pale yellow indicated the formation of Cu_2O nanospheres. The product was dried after centrifugation and washing for standby use.

20 mg of Cu_2O, 32.74 mg of 3-aminophenol and 28.4 μL ammonium sulfide solution were dispersed in 40 mL ultrapure water. 44.4 μL methanal was added to the above clarified solution for 10 min by ultrasound, and then stirred at 90 °C for 30 min. After natural cooling to room temperature, the product Cu_2O-APF was collected after washing and drying.

2.3. Preparation of Cu_2O@APF-NFC-Ab_2

2 mg of Cu_2O-APF was dissolved in 1 mL of phosphate buffered solution (PBS) (pH 7.5). 1 mL of NFC (10 μg/mL) and was added into it and vibrated for 2 h. Then 150 μL of BSA (1%) was added to the solution and continued to vibrate for 6 h. The solution was centrifuged and washed once with PBS. Then 1 mL of Ab_2 (1 μg/mL) was added and the shaking lasted for 12 h. The Cu_2O-APF@Ab_2 bioconjugate was dispersed in 1 mL PBS after centrifugation and washing.

2.4. Fabrication of the ECL immunosensor

The glassy carbon electrode (GCE) shall be polished with alumina powder to the mirror-like surface before the construction of the sensor. Firstly, 10 μL of ZT-Au was uniformly dispersed on the bright GCE surface and dried. Then the electrodes were immersed in 10 μg/mL of NFC solution for 30 min and dried. 10 μL of Ab_1, 5 μL of BSA, 10 μL of D-dimer and 10 μL of Cu_2O@APF@Ab_2 were successively dropped onto the surface of the modified electrode (Scheme 1B). It should be noted that the electrode surface should be washed with PBS after drying to remove the unbound molecules at each of the above steps.

3. Results and discussion

3.1. Characterization of ZT-Au and Cu_2O-APF

SiO_2, SiO_2–Au, ZrO_2–TiO_2–SiO_2–Au and ZT-Au were obtained successively through a series of synthesis steps. The above products were characterized by SEM and TEM. As shown in Fig. 1A and S1A, SiO_2 presented the homogeneous spherality with a diameter of about 150–180 nm. Fig. 1B and S1B showed that Au NPs were uniformly

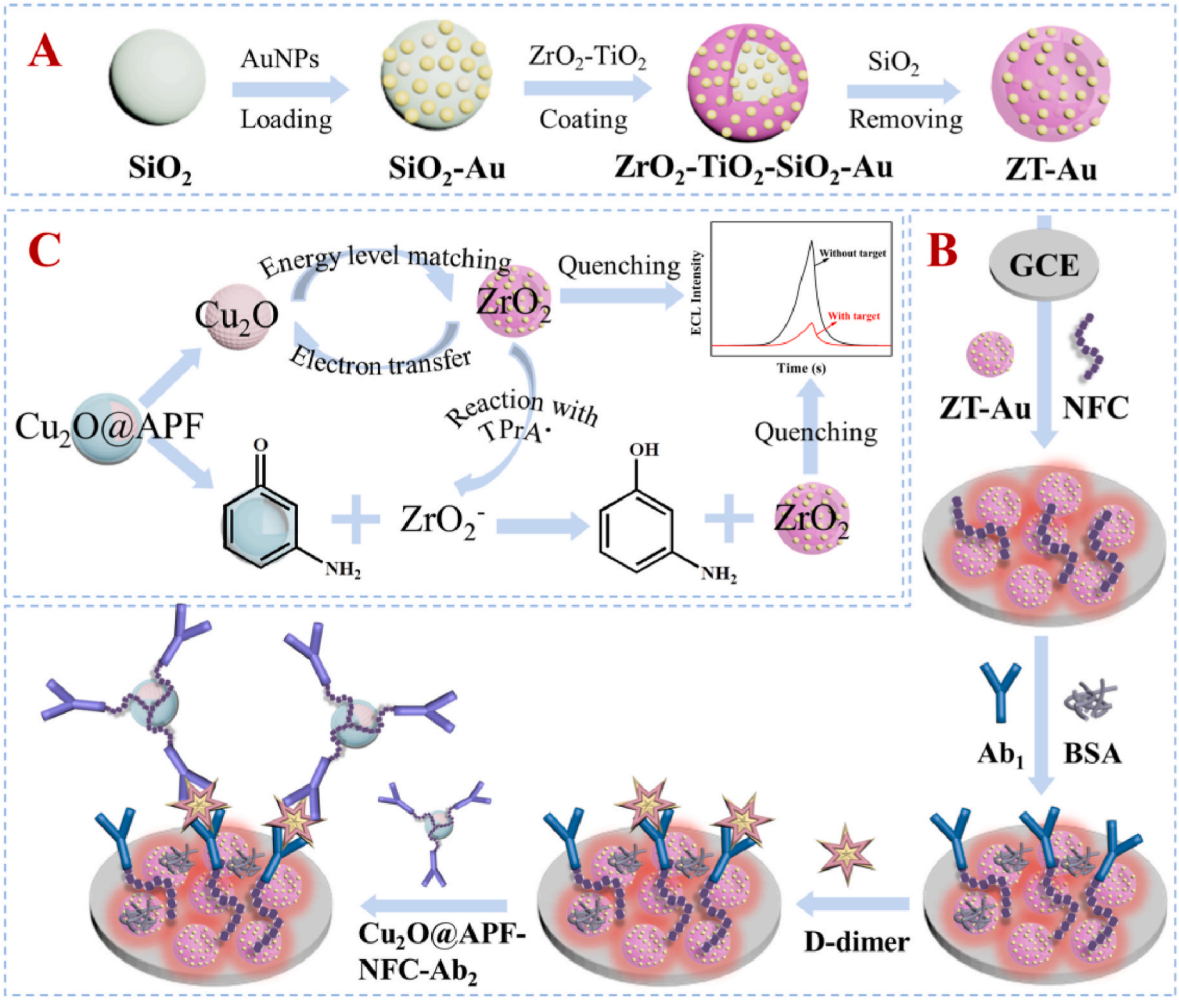

Scheme 1. (A) The synthetic process of ZT-Au; (B) The fabrication procedure of ECL immunosensor; (C) The dual-quenching mechanism of Cu_2O@APF.

loaded onto the SiO_2 surface. It was observed that the diameter of the complex enlarged visibly to about 200 nm when ZrO_2 and TiO_2 were grown on the template SiO_2 (Fig. 1C and S1C). The final product ZT-Au after the removal of SiO_2 showed the hollow nanosphere structure with the shell thickness about 10–20 nm (Fig. 1D and S1D). Mapping (Fig. 1E) and EDS (Fig. S2) diagrams confirmed that Zr, Ti, O were uniformly distributed in the hollow nanosphere, while Au elements were distributed as particles on the surface of ZT-Au. XPS was devoted to further characterizing the chemical properties and composition of ZT-Au (Fig. S3) (Feng et al., 2022; Huang et al., 2017). The binding energies of 181.9 and 184.3 eV corresponded to Zr $3d_{5/2}$ and Zr $3d_{3/2}$ of Zr^{4+}, respectively (Fig. S3A). The peaks located at 458.4 and 465.1 eV represented the Ti $2p_{3/2}$ and Ti $2p_{1/2}$ of Ti^{4+} in the complex (Fig. S3B). Two peaks with binding energies of 82.9 and 86.5 eV respectively revealed Au $4f_{7/2}$ and Au $4f_{5/2}$ levels of Au^0, which totally demonstrated the formation of Au NPs (Fig. S3C). The two peaks of O 1s at 529.9 and 531.6 eV were related to lattice oxygen of metal oxides and surface oxygen, respectively (Fig. S3D).

A comprehensive characterization of Cu_2O and Cu_2O@APF using SEM, TEM, EDS, MAPPING, XRD and XPS had been performed to validate the success of the synthesis. The Cu_2O with a size of about 80 nm displayed the morphology of uniformly distributed spheroid (Fig. 2A and B). XRD showed that Cu_2O had nicer crystallinity corresponding to the standard cubic structure of Cu_2O (JCPDS card 05–0667) (Fig. S4) (Luo et al., 2020). The lattice spacing of 0.248 in Fig. e 2C matched with curve a in Fig. 2D, both of which prove the existence of (111) crystal plane at $2\theta = 37.01$. The selected area electron diffraction image was recommended to further prove the lattice planes of Cu_2O (Fig. 2D). The XRD peaks located at 42.6, 62.4 and 74.4 correlated with crystal planes of (200), (220) and (311), which simultaneously corresponded to curves b-d in Fig. 2D through measurement and calculation.

In Fig. 2E and F, it can be observed that APF was wrapped in the outer layer of Cu_2O (indicated by the arrow in Fig. 2F) and the size of compound increased to about 100 nm. The mapping characterization of Cu_2O@APF proved the existence of Cu, O, C, N elements with uniformity of distribution (Fig. 2G). In addition, FT-IR spectroscopy was also used to characterize the outer layer APF. As shown in curve b of Fig. S5, the absorption peak at 1603 cm^{-1} was associated with the C–C stretching vibration on the benzene ring, while at 1362 cm^{-1} it was the deformation vibration of phenolic hydroxyl and at 3448 cm^{-1} it was attributed to the N–H stretching vibration. Synchronously, XPS was used to acquire the elements valence states of Cu_2O@APF (Luo et al., 2020). The peaks of 933.6 and 953.2 eV were attributed to Cu (I) $2p_{1/2}$ and Cu (I) $2p_{3/2}$ respectively, while the two shoulder peaks of 936.4 and 956.9 eV were ascribed to Cu (II) $2p_{1/2}$ and Cu (II) $2p_{3/2}$, which were caused by the slight oxidation of Cu (I) on the surface (Fig. S6A). The peak at the binding energy of 285.0 eV was concerned with C1s of benzene ring on APF (Fig. S6B). The O 1s centered at 530.4 and 532.3 eV were associated with lattice oxygen of Cu_2O and hydroxyl group oxygen of APF, respectively (Fig. S6C). The N 1s peak centered at 399.3 eV may be related to $–NH_2$ of APF (Fig. S6D).

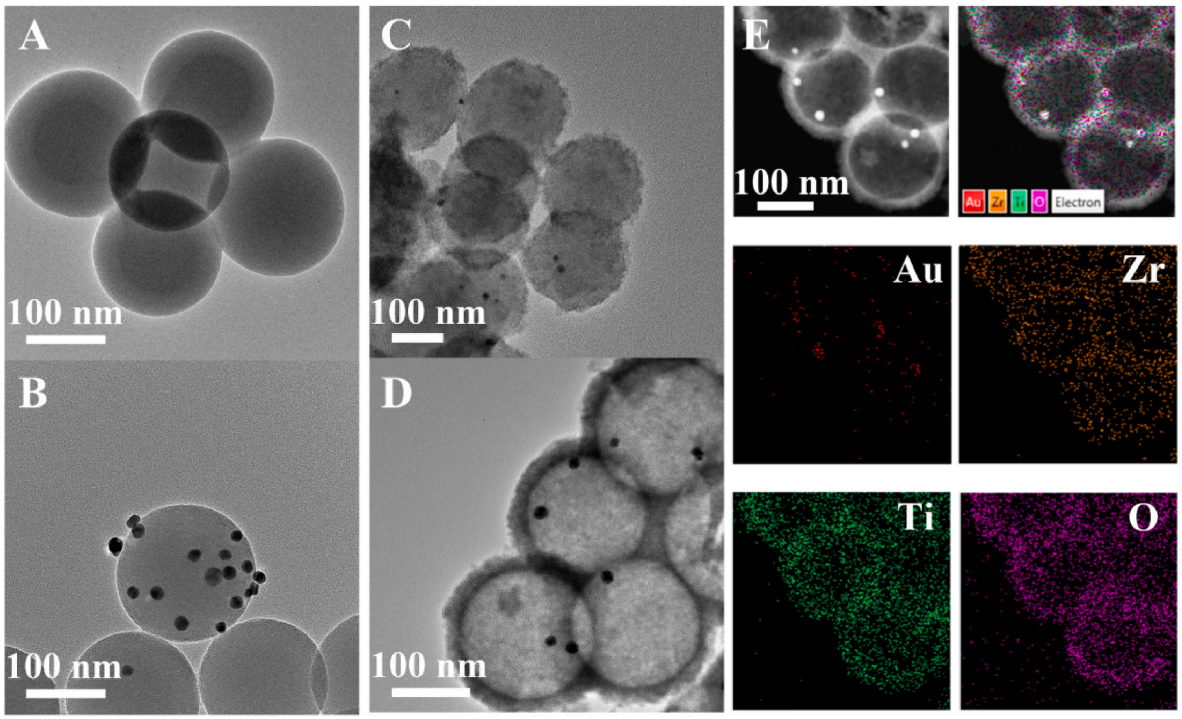

Fig. 1. TEM images of (A) SiO_2, (B) SiO_2–Au, (C) ZrO_2–TiO_2–SiO_2–Au and (D) ZT-Au; (E) mapping images of ZT-Au.

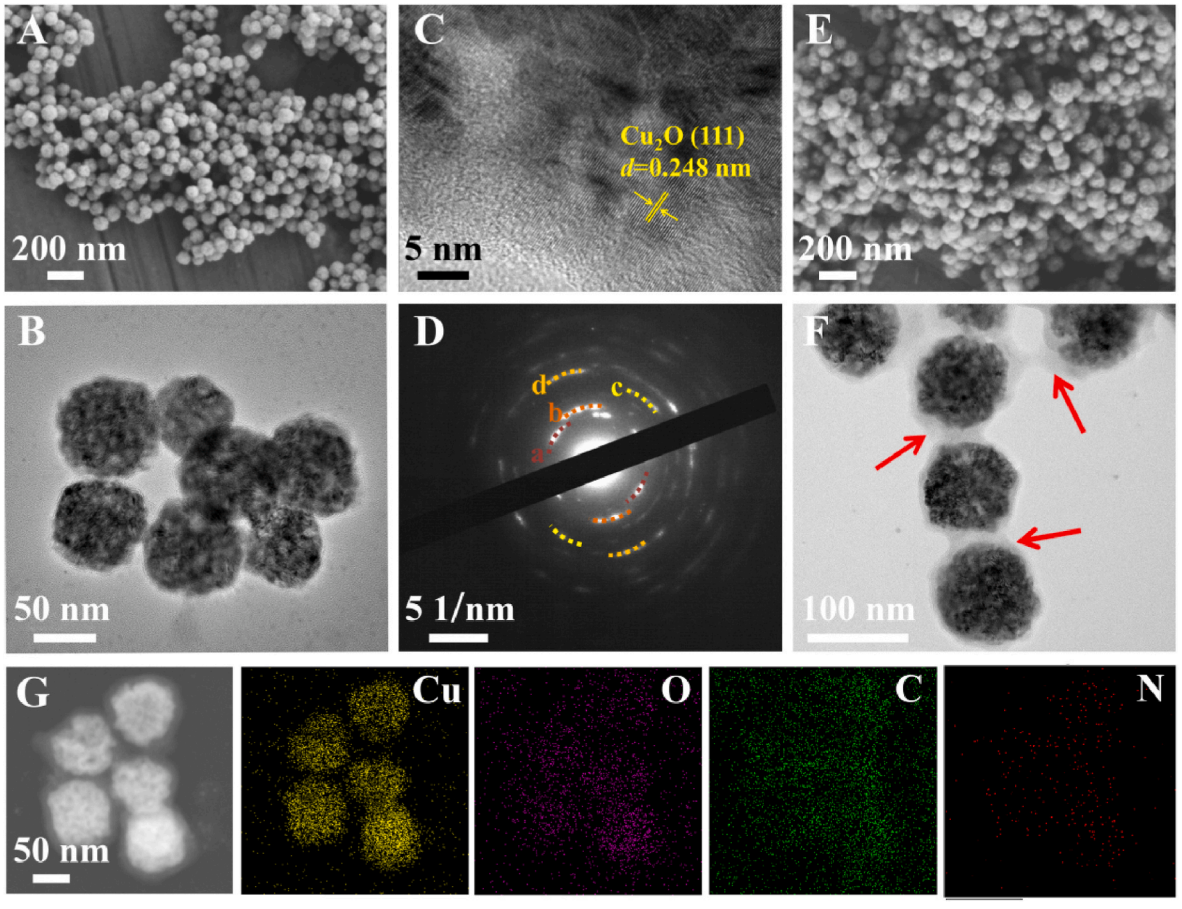

Fig. 2. (A) SEM and (B) TEM images of Cu_2O; (C) lattice fringe and (D) selected area electron diffraction image of Cu_2O; (E) SEM, (F) TEM and (G) mapping images of Cu_2O@APF.

3.2. Mechanism investigation of ECL luminescence and enhancement

The luminescence mechanism of ZrO_2 and the enhancement mechanism of TiO_2–Au had been carefully investigated and discussed. Firstly, different modified electrodes were prepared and measured to survey the change of ECL intensity (Fig.e 3A). GCE/ZrO_2 showed ECL emission of about 4000 a. u. In PBS containing 13 mmol/L TPrA (curve e). The ECL intensity of GCE/ZrO_2–TiO_2 (curve b) and GCE/ZrO_2–Au (curve c) increased to 11000 a. u. and 8000 a. u., respectively, indicating that both TiO_2 and Au NPs had the ability to enhance the ECL emission of ZrO_2. However, TiO_2–Au had no ECL response, which precluded the possibility that TiO_2–Au had ECL emission (curve f). According to the above experimental phenomena, it can be inferred that TiO_2 as the co-reaction accelerator could enhance the ECL emission of ZrO_2. When a certain voltage was applied to the modified electrode, the electrons of TiO_2 would transition from the valence band (VB) to the conduction band (CB). Meanwhile, the electrons lost by TPrA would be transferred to the corresponding holes generated on VB, which allowed TPrA to produce more of the oxidation state $TPrA^{\bullet+}$ needed for the luminescence process (Yang et al., 2021). The loading of Au NPs effectively improved the conductivity of the composite and the electronic transmission rate and thus the ECL emission of the emitter could be enhanced. In addition, GCE/ZrO_2–TiO_2–SiO_2–Au (curve d) was tested and found that its ECL signal was significantly lower than ZT-Au (curve a), which may be due to the fact that SiO_2 greatly reduced the conductivity of the composite and hindered the electron transfer in the ECL emission process. In addition, PL emission wavelength of ZrO_2 was detected at 330 nm (Fig. 4A, curve b), while the maximum emission wavelength of ECL spectrum was observed to be located at 650 nm (Fig. 4A, curve a). The redshift of 320 nm indicated the surface state emission of ZrO_2 (Dong et al., 2022). The detailed luminescence process of ZrO_2 was shown in equations a-e. Specifically, TPrA was oxidized to $TPrA^{\bullet+}$ (eq a), then deprotonated $TPrA^{\bullet}$ reacted with ZrO_2 to produce ZrO_2^- (eqs b and c), and ZrO_2^- further reacted with $TPA^{\bullet+}$ to produce excited state ZrO_2* (eq d). ECL efficiency of the emitter was also measured and calculated. Specific experimental parameters and computational methods were placed in the Supporting Information. The calculated ECL efficiency of ZT-Au was 4.8% based on the annihilation ECL efficiency of $[Ru(bpy)_3]^{2+}$ (5%), which proved that the luminophor developed in this work had a high luminescence efficiency comparable to $[Ru(bpy)_3]^{2+}$.

$$TPrA - e^- \rightarrow TPrA^{\bullet+} \text{ (a)}$$

$$TPrA^{\bullet+} - H^+ \rightarrow TPrA^{\bullet} \text{ (b)}$$

$$TPrA^{\bullet} + ZrO_2 \rightarrow ZrO_2^- \text{ (c)}$$

$$ZrO_2^- + TPA^{\bullet+} \rightarrow ZrO_2^* \text{ (d)}$$

$$ZrO_2^* \rightarrow ZrO_2 + h\nu \text{ (e)}$$

3.3. Mechanism investigation of ECL quenching

The quenching effect of Cu_2O@APF on ZT-Au had also been studied (Fig. 3B). The ECL signal of GCE/ZT-Au reached about 17000 a. u. (curve a), while the ECL signal depressed to about 10000 a. u. when Cu_2O was modified on GCE (curve b). The load of Cu_2O@APF reduced the ECL strength to about 5000 a. u. (curve c), which proved that both Cu_2O and APF had quenching effects on ZT-Au and the composites Cu_2O@APF possessed more efficient quenching. The energy level relationship between ZrO_2 and Cu_2O was calculated by UV diffuse reflection and Mott–Schottky analysis. According to Fig. 3C and D, the bandgap energy (E_g) of ZrO_2 and Cu_2O were 3.69 eV and 2.23 eV, respectively. Fig. 3E and F showed the flat-band potential (E_{fb}) of ZrO_2 and Cu_2O were −1.28 and −0.72 V, respectively, which was further extrapolated to the conduction band (CB) level (E_{cb}) of −1.24 and −0.68 V relative to NHE, respectively. Reasonable energy level matching had the opportunity of causing the electron transfer of ZrO_2 to Cu_2O, thus leading to the ECL signal quenching of ZrO_2 (Fig. S7) (Dong et al., 2022). In addition, the extremely unstable hydroxyl groups on the benzene ring of APF was easily oxidized to quinones, which may cause ZrO_2^- to revert to original state ZrO_2 after reaction with quinones and further result in ECL quenching of ZrO_2 (Qi et al., 2017).

3.4. Characterization and optimization on immunosensor construction process

Firstly, the function of peptides in the construction of immunosensor was explored. The ECL responses with and without NFC were investigated under different incubation times (Fig. 4B). The optimal incubation

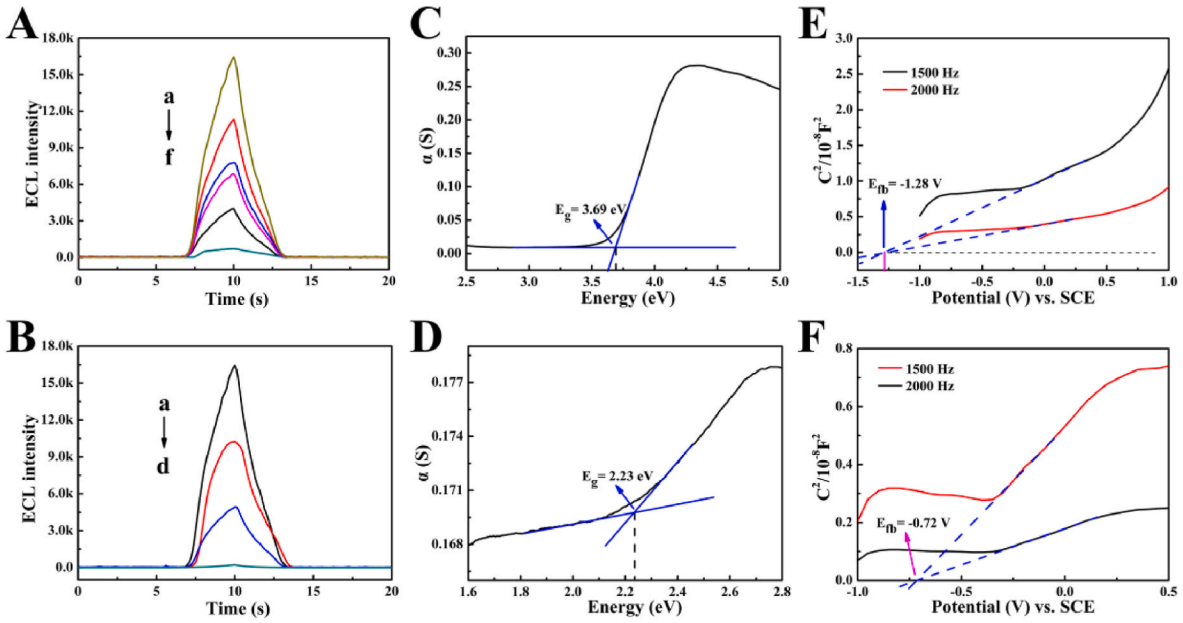

Fig. 3. (A) ECL intensity of ZT-Au (a), ZrO_2–TiO_2 (b), ZrO_2–Au (c), ZrO_2–TiO_2–SiO_2–Au (d), ZrO_2 (e), TiO_2–Au (f); (B) ECL intensity of ZT-Au (a), ZT-Au/Cu_2O (b), ZT-Au/Cu_2O@APF (c), GCE (d); UV–vis DRS diffuse-reflectance spectra of (C) ZrO_2 and (D) Cu_2O; Mott-Schottky curves of (E) ZrO_2 and (F) Cu_2O.

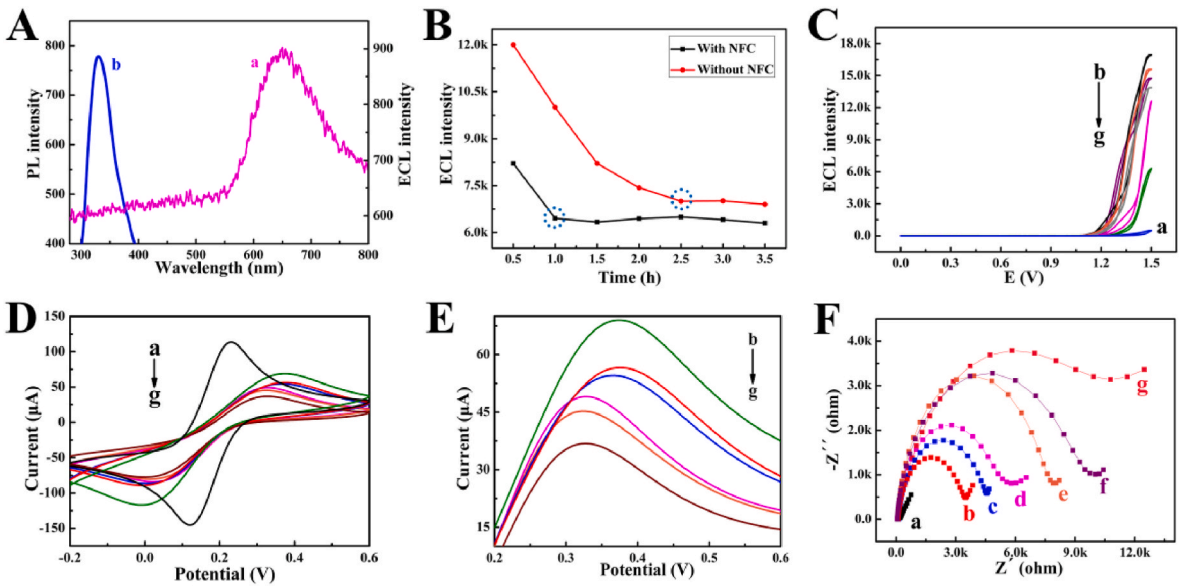

Fig. 4. (A) ECL emission spectrum (a) and PL spectrum (b) of ZT-Au; (B) ECL intensity of with NFC (a) and without NFC (b); The (C) ECL, (D and E) CV and (F) EIS of GCE (a), GCE/ZT-A u (b), GCE/ZT-Au/NFC (c), GCE/ZT-Au/NFC/BSA (d), GCE/ZT-Au/NFC/BSA/Ab_1 (e), GCE/ZT-Au/NFC/BSA/Ab_1/D-dimer (f), GCE/ZT-Au/NFC/BSA/Ab_1/D-dimer/Cu_2O@APF–NFC–Ab_2 (g).

time of antibody without NFC was 2.5 h (curve b), while the sensors constructed with NFC could achieve the optimal ECL response in 1 h incubation time (curve a). In addition, the utilization of NFC could obtain lower ECL signals compared without NFC, because the directional fixation of NFC on antibodies enabled subsequent more combination of D-dimers and quenchers (Song et al., 2021).

Characterizing the layer-by-layer modification process of sensors is an effective method to verify the success of fabrication. Herein, ECL, cyclic voltammetry (CV) and electrochemical impedance spectra (EIS) were used to characterize the gradually modified immunosensor. As shown in Fig. 4C, the bare electrode was hardly any ECL signal (curve a), whereas the ECL emission of GCE modified with ZT-Au reached 17000 a. u. (curve b). With the layer by layer modification, the ECL signal value gradually decreased (curve c-g). Similarly, the bare electrode maximized the CV current value (Fig. 4D, curve a) and minimized the impedance value (Fig. 4F, curve a). Subsequently, the current value decreased and the impedance value increased layer by layer via stepwise modification of the sensors (curve b-g). The main reason is that the incubation of biomolecules reduced the ECL signal of the substrate and electron transfer rate, which proved the successful construction of the contrivable sensor.

The optimization of influence factors is a crucial step in immunosensor design. The appropriate pH can maximize the activity of biological molecules to improve the performance of the sensor. As shown in Fig. S8A, the optimal ECL response occurred at pH 7.5, which was the optimum pH for biological molecules to remain active. Similarly, the concentration of co-reagent TPrA (Fig. S8B), ZT-Au (Fig. S8C) and Cu_2O@APF–NFC–Ab_2 (Fig. S8D) were optimized. The best performance

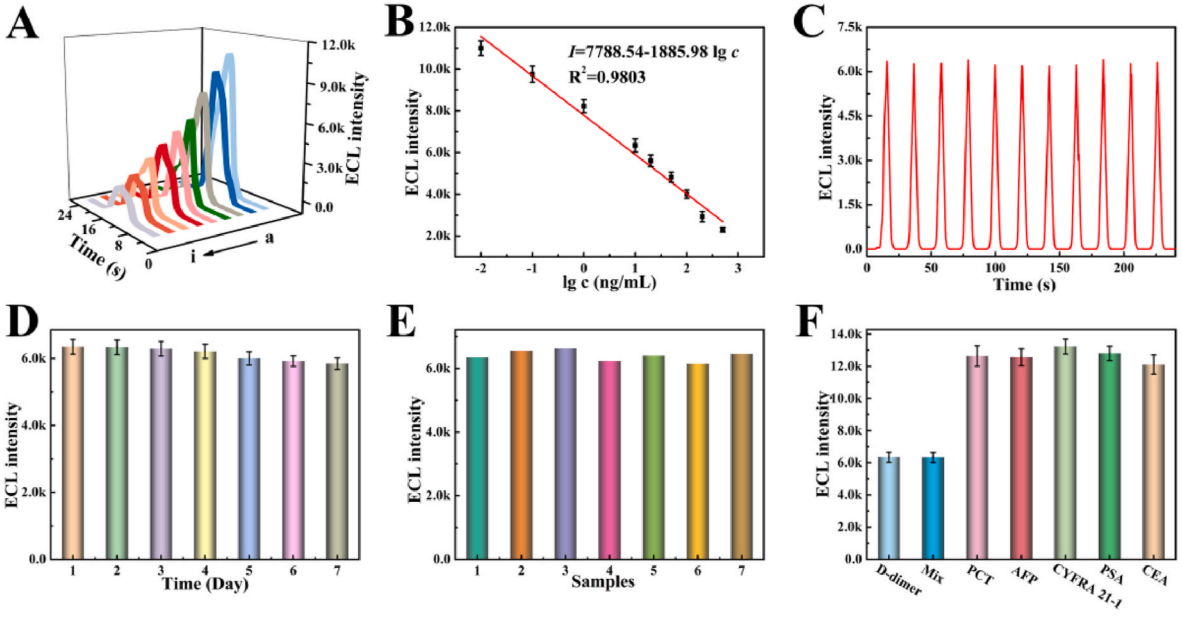

Fig. 5. (A) ECL intensity of D-dimer at different concentrations; (B) Calibration plot of D-dimer detection; (C) Long-term scanning stability, (D) long-term storage stability, (E) reproducibility and (F) specificity of immunosensor.

of fabricative immunosensor with 2 mg/mL of ZT-Au and Cu_2O@APF–NFC–Ab_2 was detected in 13 mmol/L TPrA solution. In addition, in order to ensure sufficient amount of NFC, different concentrations of NFC were optimized (Fig. S8E). The experimental results demonstrated that 10 μg/mL of NFC was sufficient for antibody binding.

3.5. Performance of ECL immunosensor

The performance of the designed immunosensor was tested with D-dimer as the detection model within the analysis range of 0.01–500 ng/mL (Fig. 5A). The calibration plot between ECL intensity and logarithm of D-dimer concentration was drawn as I = 7788.54–1885.98 lg c (R^2 = 0.9803), and the detection limit was as low as 3.6 pg/mL (Fig. 5B). This work revealed a wider detection range and lower detection limit compared with other work for D-dimer detection, which demonstrated that our work was of great significance for the sensitive detection of D-dimer (Table S1).

The stability measurement of the immunosensor was also a non-negligible work. The result of the modified electrode being scanned for 11 cycles confirmed that the stability of the immunosensor was not affected by the lengthy time scanning (Fig. 5C). In addition, a batch of immunosensors for a long time of storage were prepared and tested within 1–7 days respectively (Fig. 5D). The experimental results displayed that the ECL response of the immunosensor was still within 90% of the initial value. The testing experiment of seven modified electrodes under the same conditions manifested that the immunosensor had perfect reproducibility (Fig. 5E). The interference factors alpha fetoprotein (AFP), procalcitonin (PCT), CYFRA 21−1, prostate-specific antigen (PSA) and carcinoembryonic antigen (CEA) were introduced to carry out the specificity experiment of the sensor (Fig. 5F). Only the presence of the target D-dimer could enable the successful fabrication of the immunosensor. The above experiments explained that the immunosensor was equipped with satisfactory performance including long-term scanning stability, long-term storage stability, reproducibility and specificity.

3.6. Sample analysis

The standard addition recovery method was applied to analyze D-dimer of human plasma samples using the proposed immunosensor. The standard antigen solution containing 0.50, 1.00 and 5.00 ng/mL was added to the human plasma sample diluted 100 times to verify the recovery of immunosensor (Table S2). The results indicated a recovery rate of 97.0%–104.0% and an RSD of 2.4–3.4, demonstrating the great potential of immunosensor for practical sample analysis.

4. Conclusion

In this paper, we investigated the ECL enhancement of ZrO_2 by TiO_2 acting as a co-reaction accelerator and by AuNPs increasing the electron transport rate. ZT-Au had a high luminous efficiency of 4.8% based on the annihilation ECL efficiency of $[Ru(bpy)_3]^{2+}$ (5%). The dual-quenching effect Cu_2O@APF was introduced as Ab_2 marker to comprehensively improve the sensitivity of sensor. The utilization of polypeptide NFC not merely ensured the active site of antigen, but also saved the time required for immunosensor construction. The constructed immunosensor was equipped with favorable performance and exhibited potential application capability in the detection of human plasma samples.

CRediT authorship contribution statement

Xue Dong: Conceptualization, Data curation, Writing – original draft. **Xiaoyue Zhang:** Methodology, Writing – review & editing. **Yu Du:** Funding acquisition. **Jiajun Liu:** Experimental operation. **Qingze Zeng:** Experimental operation. **Wei Cao:** Funding acquisition, Writing – review & editing. **Qin Wei:** Funding acquisition, Project administration. **Huangxian Ju:** Funding acquisition, Formal analysis.

Declaration of competing interest

The authors declare that they have no known competing financial interests or personal relationships that could have appeared to influence the work reported in this paper.

Data availability

The authors do not have permission to share data.

Acknowledgments

This study was supported by the National Natural Science Foundation of China (Nos. 22206056, 22274062), the Shandong Provincial Natural Science Foundation (Nos. ZR2022QB117, ZR2022MB089), the Special Foundation for Taishan Scholar Professorship of Shandong Province (No. ts20130937). The authors thank Yankai Li from Shiyanjia Lab (www.shiyanjia.com) for XPS analysis.

Appendix A. Supplementary data

Supplementary data to this article can be found online at https://doi.org/10.1016/j.bios.2023.115437.

References

Adebayo, B.O., Yu, H., Rownaghi, A.A., Liang, X., Rezaei, F., 2022. Chem. Eng. J. 444, 136603.
Chen, C., Hildebrandt, N., 2020. Trac-Trend. Anal. Chem. 123, 115748.
Cui, Y., Jin, Y., Chen, X., Wu, J., 2018. ACS Sens. 3, 1439–1444.
Dong, X., Zhao, G., Li, Y., Zeng, Q., Ma, H., Wu, D., Ren, X., Wei, Q., Ju, H., 2022. Anal. Chem. 94, 12742–12749.
Favaloro, E.J., Thachil, J., 2020. Clin. Chem. Lab. Med. 58, 1191–1199.
Feng, G., Hu, M., Wu, B., Shi, S., Yuan, S., Li, Y., Zeng, H., 2022. Nanomaterials 12, 742.
Gao, H., Wei, X., Li, M., Wang, L., Wei, T., Dai, Z., 2021. Small 17, 2103424.
Hu, L., Wu, Y., Xu, M., Gu, W., Zhu, C., 2020. Chem. Commun. 56, 10989–10999.
Huang, J., Liu, J., Tian, L., Li, X., Ma, X., Yu, X., Guo, Q., Zhao, J., 2021. Chem. Eng. J. 412, 128621.
Huang, M., Zhang, Y., Zhou, Y., Zhang, C., Zhao, S., Fang, J., Gao, Y., Sheng, X., 2017. J. Colloid Interface Sci. 497, 23–32.
Jia, Y., Yang, L., Xue, J., Zhang, N., Fan, D., Ma, H., Ren, X., Hu, L., Wei, Q., 2019. ACS Sens. 4, 1909–1916.
Jin, Z., Zhu, X., Wang, N., Li, Y., Ju, H., Lei, J., 2020. Angew. Chem., Int. Ed. 59, 10446–10450.
Kagalwala, H.N., Reeves, R.T., Lippert, A.R., 2022. Curr. Opin. Chem. Biol. 68, 102134.
Ledsgaard, L., Ljungars, A., Rimbault, C., Sorensen, C.V., Tulika, T., Wade, J., Wouters, Y., McCafferty, J., Laustsen, A.H., 2022. Drug Discov. Today 27, 2151–2169.
Li, B., Tan, H., Jenkins, D., Raghavan, V.S., Rosa, B.G., Guder, F., Pan, G., Yeatman, E., Sharp, D.J., 2020. Carbon 168, 144–162.
Li, X., Lu, Z., Wang, T., 2021. Nano Res. 14, 1233–1243.
Li, Z., Zhang, J., Huang, Y., Zhai, J., Liao, G., Wang, Z., Ning, C., 2022. Coord. Chem. Rev. 471, 214723.
Liu, Y., Li, B., Zhang, H., Liu, Y., Xie, P., 2022. Coord. Chem. Rev. 457, 214416.
Luo, X., Hu, H., Pan, Z., Pei, F., Qian, H., Miao, K., Guo, S., Wang, W., Feng, G., 2020. J. Hazard Mater. 396, 122735.
Lupu, L.-M., Wiegand, P., Holdschick, D., Mihoc, D., Maeser, S., Rawer, S., Voelklein, F., Malek, E., Barka, F., Knauer, S., Uth, C., Hennermann, J., Kleinekofort, W., Hahn, A., Barka, G., Przybylski, M., 2021. Int. J. Mol. Sci. 22, 12832.
Ma, C., Cao, Y., Gou, X., Zhu, J.-J., 2020. Anal. Chem. 92, 431–454.
Mohan, B., Kumar, S., Kumar, V., Jiao, T., Sharma, H.K., Chen, Q., 2022. Trac-Trend. Anal. Chem. 157, 116735.
Ordieres-Ortega, L., Demelo-Rodriguez, P., Galeano-Valle, F., Kremers, B.M.M., ten Cate-Hoek, A.J., ten Cate, H., 2020. Thromb. J. 189, 5–12.
Qi, B.-P., Zhang, X., Shang, B.-B., Xiang, D., Qu, W., Zhang, S., 2017. Carbon 121, 72–78.
Qu, B., Sun, J., Li, P., Jing, L., 2022. J. Hazard Mater. 425, 127990.
Rao, D., Mei, K., Yan, T., Wang, Y., Wu, W., Chen, Y., Wang, J., Zhang, Q., Wu, S., 2022. Nano Res. 15, 1003–1012.
Sabzehmeidani, M.M., Kazemzad, M., 2022. Sci. Total Environ. 810, 151997.
Silva, J.P.B., Sekhar, K.C., Pan, H., MacManus-Driscoll, J.L., Pereira, M., 2021. ACS Energy Lett. 6, 2208–2217.
Sobhanie, E., Salehnia, F., Xu, G., Hamidipanah, Y., Arshian, S., Firoozbakhtian, A., Hosseini, M., Ganjali, M.R., Hanif, S., 2022. Trac-Trend. Anal. Chem. 157, 116727.

Song, X., Wu, T., Luo, C., Zhao, L., Ren, X., Zhang, Y., Wei, Q., 2021. Anal. Chem. 93, 13045–13053.
Sueda, S., 2022. Anal. Sci. 38, 1–2.
Sugita, T., Katayama, M., Okochi, M., Kato, R., Ichihara, T., Honda, H., 2013. Biochem. Eng. J. 79, 33–40.
Tian, D., Wang, J., Zhuang, Q., Wu, S., Yu, Y., Ding, K., 2023. Food Chem. 404, 134183.
Tian, Y., Du, L., Zhu, P., Chen, Y., Chen, W., Wu, C., Wang, P., 2021. Biosens. Bioelectron. 176, 112899.
Wei, J., Chen, L., Cai, X., Lai, W., Chen, X., Cai, Z., 2022. Biosens. Bioelectron. 216, 114664.
Winczewski, J., Herrera, M., Cabriel, C., Izeddin, I., Gabel, S., Merle, B., Arce, A.S., Gardeniers, H., 2022. Adv. Opt. Mater. 10, 2102758.
Yang, K., Lee, E.B., Lee, D.H., Park, J.Y., Kim, S.H., Park, G.H., Yu, G.T., Lee, J.I., Kim, G. H., Park, M.H., 2022. Compos. B Eng. 236, 109824.
Yang, L., Wu, T., Du, Y., Zhang, N., Feng, R., Ma, H., Wei, Q., 2021. Anal. Chem. 93, 16906–16914.
Ye, Q.-N., Wang, Y., Shen, S., Xu, C.-F., Wang, J., 2021. Adv. Healthcare Mater. 10, 2002139.
Yu, W., Zhao, L., 2021. Trac-Trend. Anal. Chem. 136, 116197.
Yuan, C., Li, M., Wang, M., Cao, H., Lin, T., 2021. Electrochim. Acta 390, 138798.
Zhao, R., Su, Z., Komissarov, A.A., Liu, S.-L., Yi, G., Idell, S., Matthay, M.A., Ji, H.-L., 2021. Front. Immunol. 12, 691249.
Zhao, Y., Bouffier, L., Xu, G., Loget, G., Sojic, N., 2022. Chem. Sci. 13, 2528–2550.